DESIGN AND TESTS OF A FLEXIBLE SAILWING AIRFOIL FOR LIGHTWEIGHT AIRCRAFT

L.M.M. Boermans and P.C.M. van den Borne,
Delft University of Technology, Department of Aerospace Engineering, The Netherlands
Presented at the 19th OSTIV Congress, Rieti, Italy (1985)

1. Introduction

At the Delft University of Technology Low Speed Laboratory (LSL) an investigation was performed to design and test a flexible airfoil for sailwing application. The sailwing, Fig. 1, consists of a rigid leading edge spar, tip and root ribs, a trailing edge cable and a cloth membrane wrapped around the leading edge and attached to the trailing edge, forming the upper and lower sail surfaces. Since the introduction of the sailwing by Princeton University in 1948 (1) several theoretical and experimental investigations have been performed (2,3,4,5,6). Among the results obtained the following are of particular interest.

The present investigation is focussed on the theoretical design and experimental verification of a flexible airfoil for such a sailwing application.
Several tools were used:
- the trailing edge cable deflections and tensions of the airloaded sailwing were calculated according to the procedure given by Ormiston (3);
- the flexible airfoil shapes and pressure distributions were calculated by the iteration method developed by den Boer (6), and the aerodynamic characteristics were calculated by the LSL airfoil analysis and design computer program (7);

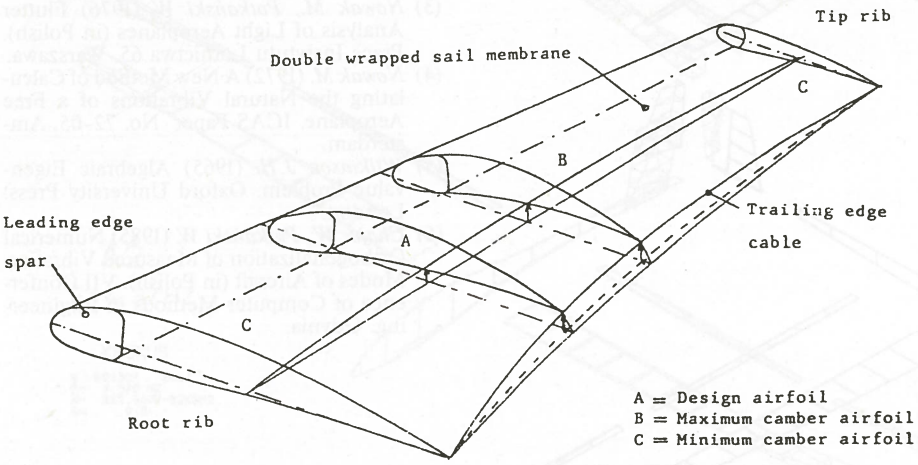

Fig. 1. Sailwing concept.

Due to aerodynamic loading the trailing edge cable deflects forward and upward between the fixed root and tip attachment points, leading to a reduction of angle of attack and increase of the amount of camber for the unsupported wing sections in between. As a result, the span lift distribution and induced drag is substantially comparable to the rigid wing and close to that of the elliptical optimum. Unlike many flexible wing designs, the membrane tension produced by the pretensioned trailing edge cable provides stability to the sail surfaces, thus allowing the sailwing to operate smoothly through conditions of positive and negative lift.
The light weight, simple construction, low costs and good aerodynamic performance make the sailwing suitable for low-speed applications as windmills, sailing-boats, hang-gliders, ultralights or light-weight sailplanes (which might bridge the gap between the performance of hang-gliders and modern sailplanes).

- the tests were performed in the low-speed low-turbulence windtunnel of the Department of Aerospace Engineering at Delft University of Technology.

2. Airfoil design

Main design parameters, which can effectively be used for the design of flexible airfoils are the shape of the rigid leading edge spar and the lengths of the upper and lower surface membranes. They will be discussed in this section, followed by some viscous flow calculation results.

Leading edge spar

An important criterion in the design of the rigid leading edge is to postpone suction peaks up to high angles of attack. Also, for drag reasons, discontinuities in curvature at the points where the membranes separate from the spar should be avoided. Since in practical sailwing application the vertical deflection of the membranes and consequently their point of separation varies along the wing span, a certain chordwise variation of the membrane separation point has to be taken into account. A third aspect, defining the chordwise extent of the spar, is of structural nature, since the membranes and trailing edge cable introduce a bending moment in the spar of which the major component is acting in the plane of the wing.
The most simple leading edge spar from manufacturing point of view is a circular tube. Fig. 2 presents a typical pressure distribution for this type of leading edge, showing undesirable suction peaks on the nose. Many attempts, using inclined elliptical and superelliptical cross sections, eventually with different upper and lower surface contour, did not yield desirable pressure distributions. Similar results were obtained by Murai and Maruyama (4); they recommend to use the nose shape of the NACA 6412 airfoil. This airfoil has a concave lower surface, which is typical for a flexible airfoil, and its shape is defined by some mathematical expressions, thus meeting the requirements for the description of the nose shape in the flexible airfoil computer program developed by den Boer. In order to obtain a smooth flexible airfoil shape without dis-

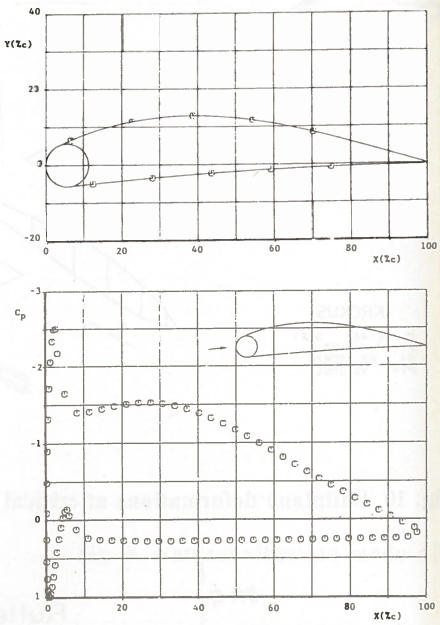

Fig. 2. Shape and pressure distribution of a flexible airfoil with circular nose shape.

continuity in curvature at the membrane separation area a suitable transition to the rearward part of the spar had to be designed. The resulting shape of the rear part, shown in fig. 3, can be expressed by polynomials where constraints in the form of continuity of the first and second derivative of the leading edge contour were imposed upon the design of the transition area. It was decided to limit the chordwise extent of the leading edge spar to about 20% of the chord.

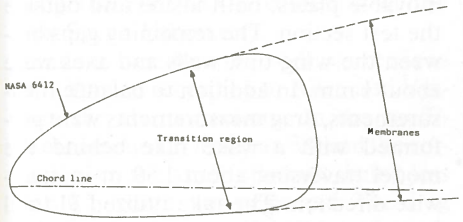

Fig. 3. Design shape of leading edge spar.

Flexible part

For the design of the flexible part some basic wing design parameters have to be specified first. For present purpose, a sailwing with an aspect ratio of 8.5, to be used for hang-glider application (wing loading 75 N/m^2), was chosen. At rest the trailing edge has a parabolic shape and the cable pre-tension imparts a constant chordwise sail pre-tension along the span (the trailing edge design shape parameter as defined by Ormiston (3) is 0.2). Under steady flight conditions, where the speed is related to the lift coefficient such that the aerodynamic load is constant, it may be assumed that the additional cable deflection and elongation of the membranes is independent of the angle of attack. Taking the unknown internal wing pressure equal to the ambient pressure, the design problem is reduced to finding the optimum membrane lengths, in relation to aerodynamic performance and required cable pre-tension, at all stations along the span.

The flexible double membrane airfoil computer program and the LSL airfoil analysis and design computer program were used extensively for this purpose. First the sailwing "average" airfoil section, denoted by A in Fig. 1, was studied; the design lift coefficient was 1.0 at a Reynolds number of 0.9×10^6. Next, taking into account the horizontal and vertical deflection of the trailing edge cable along the span, the maximum and minimum camber sections, denoted by B and C in Fig. 1, were checked.

It appeared that favourable pressure distributions for extensive laminar flow on the *upper surface* could be achieved by using a slackness - defined in Fig. 4 - of about 1.5%, i.e. a total upper sail length of 104.7% chord. The membrane tension was found to be almost independent of the slackness and amounted to about 110

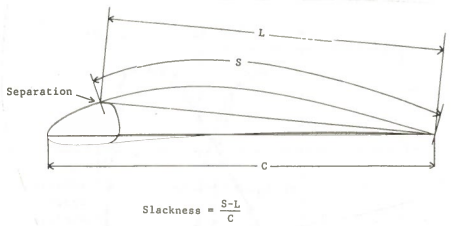

Fig. 4. Definition of slackness.

N/m. At the *lower surface* smooth pressure distributions for laminar flow up to the trailing edge could be achieved at all stations along the span by reducing the slackness below 0.06% to 0.07% (total sail length 101.2%c), resulting in a membrane tension of about 170 N/m. Due to the small camber the membrane tension is very sensitive to slackness.

Because of the different upper and lower surface membrane tensions the sail cloth has to be fixed at the leading edge, for instance in the way a sail is fixed to the mast of a sailing-boat. This will introduce some local disturbances which might cause turbulent flow. A theoretical analysis based on the critical roughness Reynolds number concept showed that a maximum roughness height of 0.1% chord is permitted to preserve laminar flow provided that its position is at 1.5%c of the lower surface (i.e. just behind the stagnation point at high angles of attack). The trailing edge cable tension and consequently the spanwise sailwing camber are dictated by the lower surface slackness only; a cable pretension of about 4 kN is required.

The final design airfoil shape and pressure distribution at $\alpha = 5°$ is presented in Fig. 5 together with the NACA 6412 shape and pressure distribution. Fig. 6 illustrates how the flexible shape changes with angle of attack.

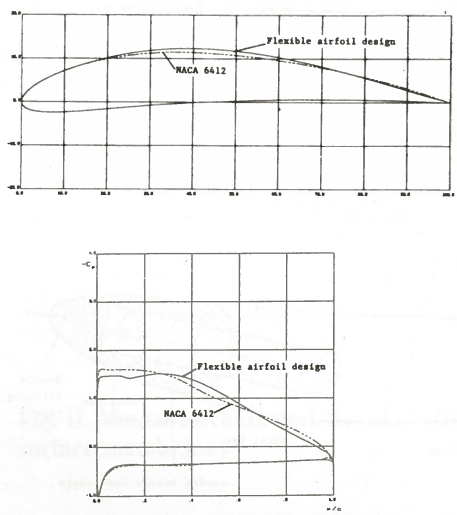

Fig. 5. Shape and pressure distribution of the flexible airfoil design (calculated, $C_{Pint} = 0$) and rigid NACA 6412 at $\alpha = 5°$.

Viscous flow calculation results

Fig. 7 presents the aerodynamic characteristics of the flexible airfoil design and the rigid NACA 6412 airfoil as calculated for constant load Reynolds numbers according to $Re = 0.9 \times 10^6/\sqrt{C_l}$ by the LSL airfoil analysis and design computer program.

The general behaviour of the flow is similar for both airfoils. If the lift coefficient is reduced the boundary layer transition position on the lower surface moves rapidly forward at $C_l \approx 0.8$ causing an increase of the drag coefficient. At lift coefficients above 0.8 the lower surface is completely laminar. On the upper surface of the flexible airfoil the transition position gradually moves forward with increasing lift coefficient, starting at some 60%c. The difference in pressure distributions, indicated in Fig. 5, causes earlier transition on the upper surface of NACA 6412 at positive lift coefficients and consequently a higher drag coefficient. The maximum lift coefficient of the flexible airfoil is predicted slightly higher than for the NACA airfoil.

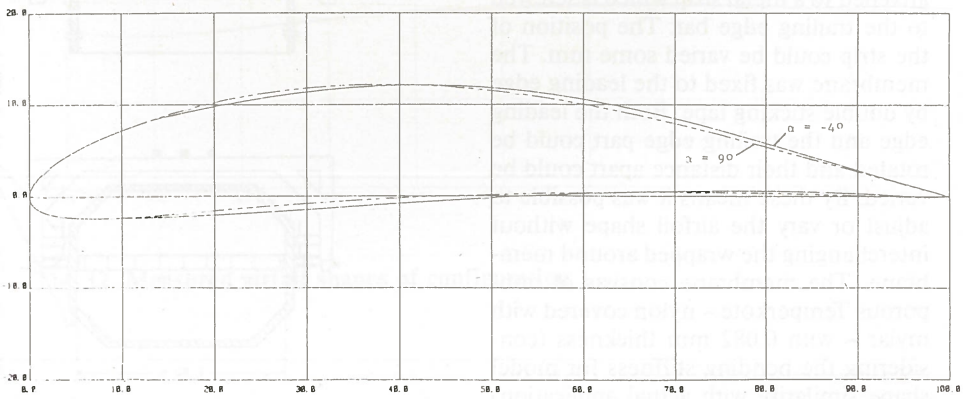

Fig. 6. Calculated flexible design airfoil shapes; $C_{Pint} = 0$.

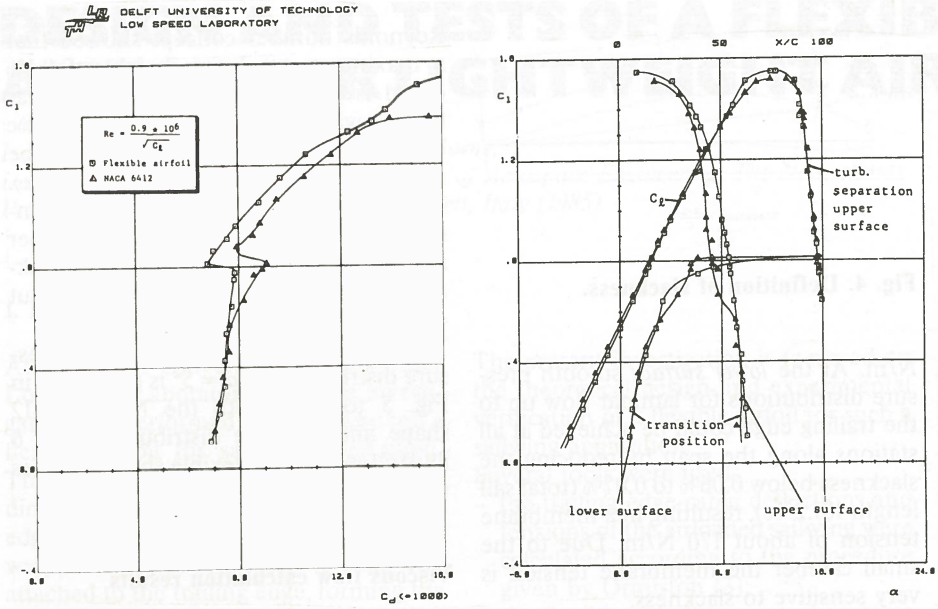

Fig. 7. Calculated characteristics of the flexible airfoil design ($C_{Pint} = 0$) and the rigid NACA 6412 airfoil.

3. Windtunnel tests

Model

The two-dimensional model spanned the width of the test section (1.80 m) and had an adjustable chord length of about 0.36 m. As shown in the cross-section, Fig. 8, the nose part consists of a metal bar and a wooden leading edge shaped according to the design. The rear part is built up of a tapered aluminum trailing edge bar and a metal box to prevent bending due to membrane tension. The membrane is wrapped around the leading edge and attached to a metal strip which is screwed to the trailing edge bar. The position of the strip could be varied some mm. The membrane was fixed to the leading edge by double sticking tape. Both the leading edge and the trailing edge part could be rotated and their distance apart could be varied. By these means it was possible to adjust or vary the airfoil shape without interchanging the wrapped around membrane. The membrane consists of non-porous Temperkote - nylon covered with mylar - with 0.082 mm thickness (considering the bending stiffness for model shape similarity with actual application) and 0.78 N/m^2 weight.

At the mid-span and at every 200 mm span position black lines were drawn in chordwise direction on both sides of the model, to enable the determination of the airfoil shape.

Windtunnel, model support and test equipment

The low-speed low-turbulence windtunnel is of the closed return type and has an interchangeable octagonal test section 1.80 m wide and 1.25 m high, Fig. 9. The turbulence level in the test section varies from about 0.015% at 15 m/s to 0.03% at 50 m/s.

The model leading edge and trailing edge axes passed through the tunnel walls and were attached to a frame such that the airfoil shape and/or the angle of attack could be changed. The frame was suspended to the six component balance system of the windtunnel. The openings in the tunnel walls were covered by thin movable plates, both inside and outside the test section. The remaining gaps between the wing tips, walls and axes were about 1 mm. In addition to balance measurements, drag measurements were performed with a wake rake behind the model traversing about 1.50 m in spanwise direction. The rake utilized 31 total pressure tubes and 4 static pressure tubes. A pitot-static tube was mounted on the tunnel floor. The internal pressure of the airfoil was measured by a thin tube which could be traversed inside the model through a hole in the tunnel side wall.

All pressures were recorded by an automatically reading multi-tube liquid manometer. Transition of the boundary layer was detected by a stethoscope, and flow separation was studied with a handheld tuftwand.

The black lines on the model surface were photographed through perspex windows in the tunnel walls by two cameras at a fixed position, Fig. 9.

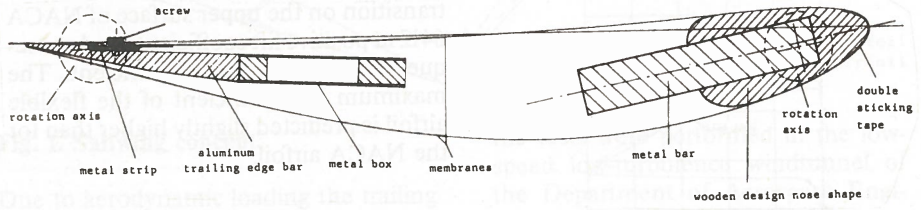

Fig. 8. Cross-section of the windtunnel model.

Tests

During preliminary tests the membrane appeared to shift slightly over the leading edge after some running time, thus changing the intended slacknesses. To eliminate this, the airfoil characteristics were measured at constant load Reynoldsnumbers according to $Re_c = 0.6 \times 10^6/\sqrt{C_l}$ instead of $Re_c = 0.9 \times 10^6/\sqrt{C_l}$.

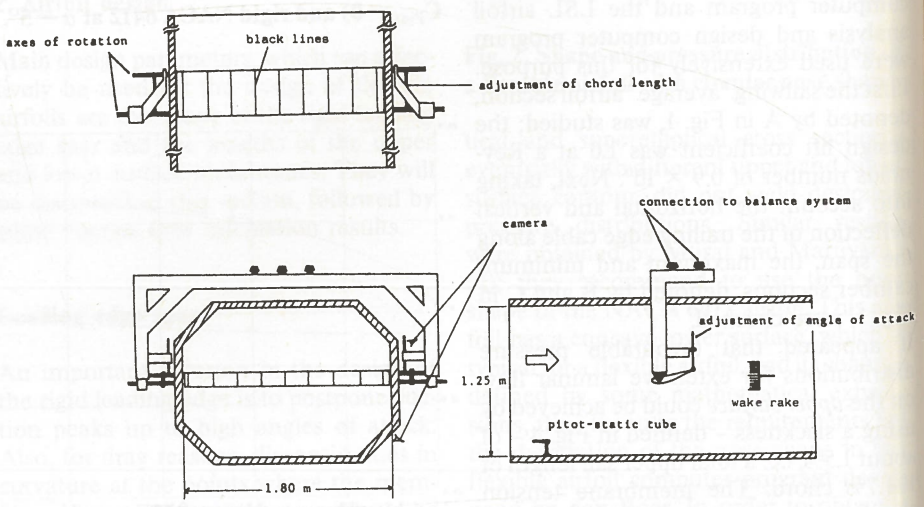

Fig. 9. Test set-up.

Two airfoil configurations were measured. Configuration 1 corresponded to the design specifications and configuration 2 had a 0.5%c longer upper surface membrane to test the sensitivity of the characteristics for upper surface slackness.

Data reduction

All balance and wake rake data were on line reduced and the lift, drag and pitching-moment coefficients were plotted using the HP21MX-E computer of the Low Speed Laboratory.
Standard windtunnel wall corrections were applied according to Allen and Vincenti (8); the corrections on the coefficients amount to less than 3% and the correction on the angle of attack, being less than 0.1 degree, was neglected. The drag due to wing-tip tunnel-wall interference was derived from the difference between balance and wake rake traverse measurements at several angles of attack, similar to the procedure described in Ref. 9. Fig. 10 shows an example for $\alpha = 0°$. The wake drag distribution shows peaks due to the screws on the lower surface trailing edge; a mean drag value was calculated by a least square method. The differences in drag when compared with the balance measurements were plotted against the lift coefficient squared, showing an almost straight line. All balance measurements were corrected for wing-tip tunnel-wall interference by taking into account a drag value according to this relationship. The airfoil shape was determined from the photographs. According to the procedure described in Ref. 6, in addition to these pictures, a sheet of millimeterpaper at the same spanwise position as the black lines on the model was photographed after the model was removed, hence the distortion due to the perspex windows and camera positions is known. By projecting the pictures of the black lines on the corresponding pictures of the millimeterpaper, the airfoil coordinates were determined.

Results

Fig. 11 shows the measured airfoil characteristics of configuration 1 and 2. Comparison with Fig. 7 shows that the predicted trends are in agreement with the measurements; for instance the lower surface has laminar flow above a certain lift coefficient (as confirmed by stethoscope measurements). Due to the increased camber, configuration 2 shows slightly higher lift and pitching-moment coefficients than configuration 1, but no higher maximum lift coefficient. The maximum lift coefficient is 1.54 at $\alpha = 12°$ for configuration 1 and 1.49 at $\alpha = 10.5°$ for configuration 2, both at $Re_c = 0.5 \approx 10^6$.

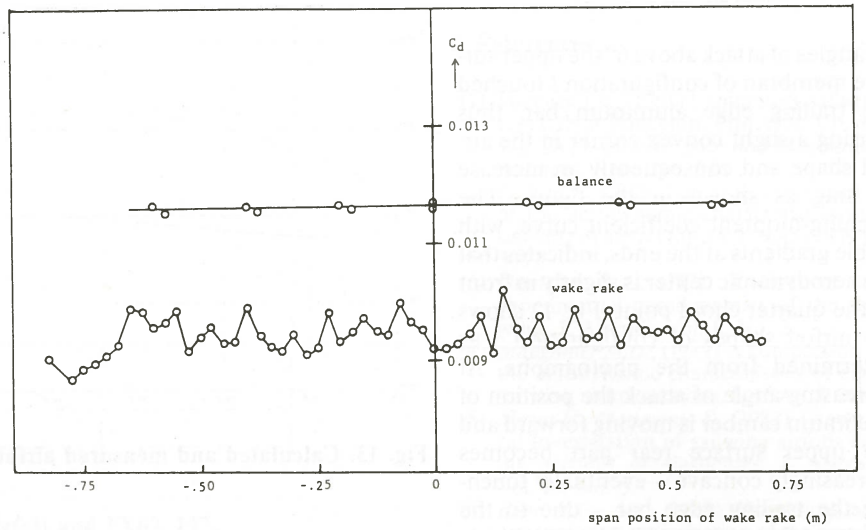

Fig. 10. Wake rake traverse and balance measurements at $\alpha = 0°$.

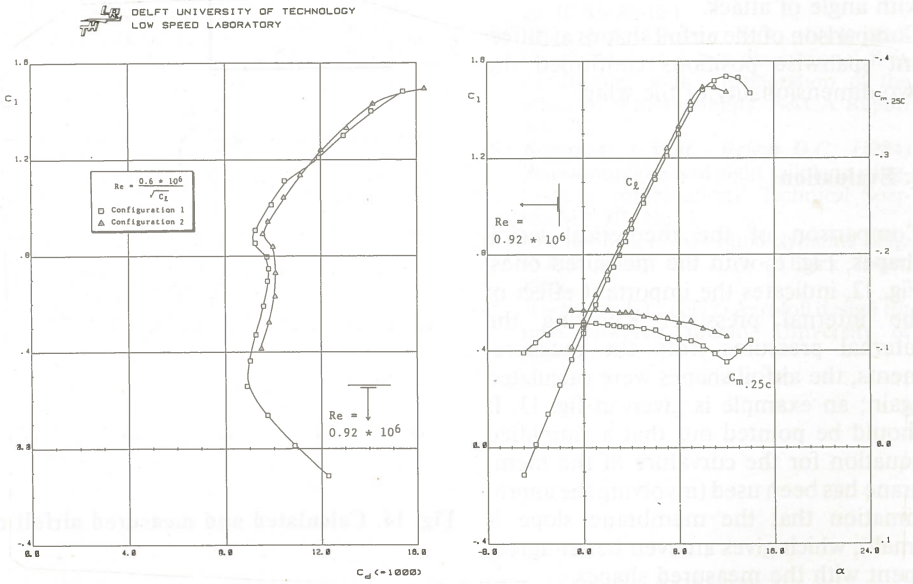

Fig. 11. Measured characteristics of configuration 1 (design) and 2 (0.5%c longer upper surface membrane).

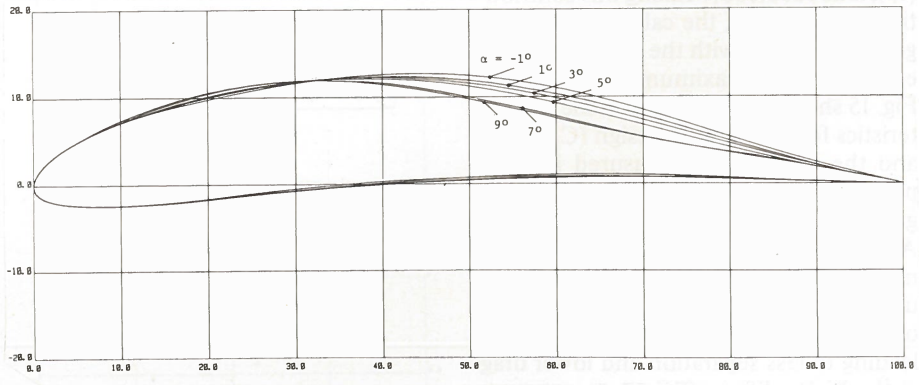

Fig. 12. Measured airfoil shapes of configuration 1.

At angles of attack above 6° the upper surface membran of configuration 1 touched the trailing edge aluminum bar, thus causing a slight convex corner in the airfoil shape and consequently an increase in drag as shown in the figure. The pitching-moment coefficient curve, with stable gradients at the ends, indicates that the aerodynamic center is slightly in front of the quarter chord point. Fig. 12 shows the airfoil shapes of configuration 1 as determined from the photographs. At increasing angle of attack the position of maximum camber is moving forward and the upper surface rear part becomes increasingly concave - eventually touching the trailing edge bar - due to the change of pressures outside and inside the airfoil, as will be shown later. (The measured internal pressure coefficient decreases linearly from -0.05 at $\alpha = -4°$ to -0.45 at $\alpha = -12°$). The shape of the taut lower surface membrane hardly changes with angle of attack.
Comparison of the airfoil shapes at different spanwise positions confirmed the two-dimensionality of the wing.

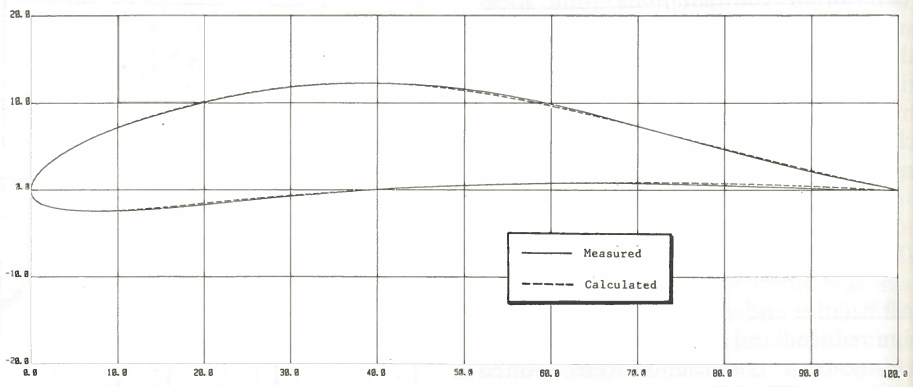

Fig. 13. Calculated and measured airfoil shape at α 3°; $C_{Pint} = -.225$.

4. Evaluation

Comparison of the theoretical airfoil shapes, Fig. 6, with the measured ones, Fig. 12, indicates the important effect of the internal pressure. Knowing the internal pressures from the measurements, the airfoil shapes were calculated again; an example is given in fig. 13. It should be pointed out that a simplified equation for the curvature of the membrane has been used (involving the approximation that the membrane slope is small), which gives an even better agreement with the measured shapes.
Fig. 14 shows the corresponding recalculated aerodynamic characteristics in comparison with the measurements. The drag increment due to the 23 screws at the lower surface, as estimated from Hoerner (10), is about 0.0007. Taking this contribution into account, the calculations are in good agreement with the measurements, except near the maximum lift coefficient.
Fig. 15 shows a comparison of the characteristics for the original design ($C_{Pint} = 0$) and the shapes with measured internal pressure ($C_{Pint} > 0$), calculated at the original constant load Reynolds numbers. Apart from the discrepancy near maximum lift, the pressure induced concave upper contour is favourable for the development of the turbulent boundary layer, leading to less separation and lower drag at the higher lift coefficients.
Finally, Fig. 16 compares the sinking speed ratio of the flexible airfoil and the well-known low Reynolds number airfoil FX63-137, designed for man-powered aircraft (11), indicating the high level of performance of the flexible design.

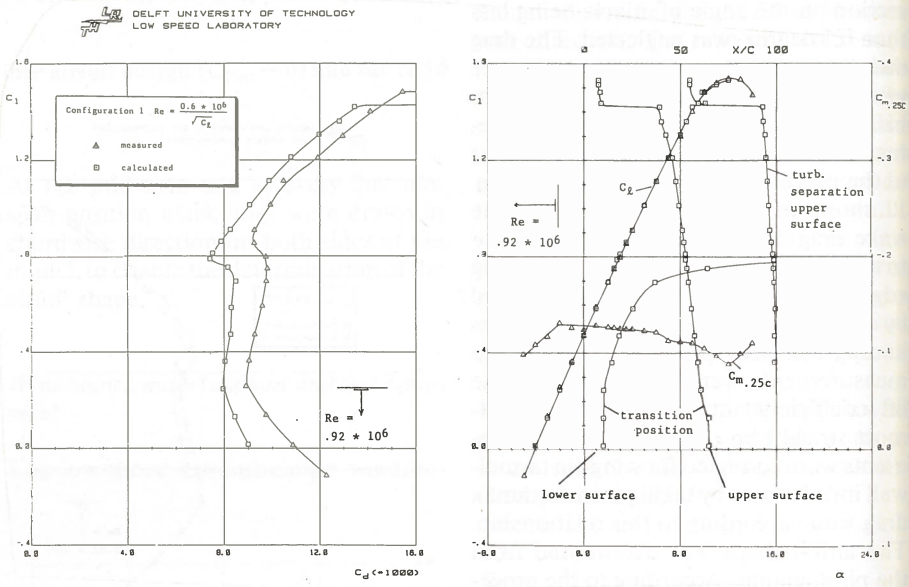

Fig. 14. Calculated and measured airfoil characteristics ($C_{Pint} < 0$).

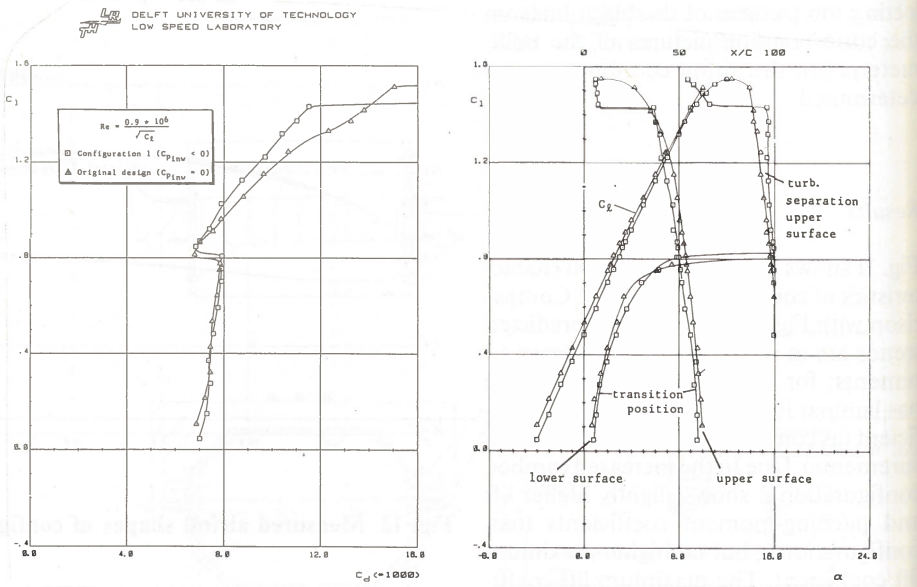

Fig. 15. Comparison of calculated characteristics, effect of internal pressure.

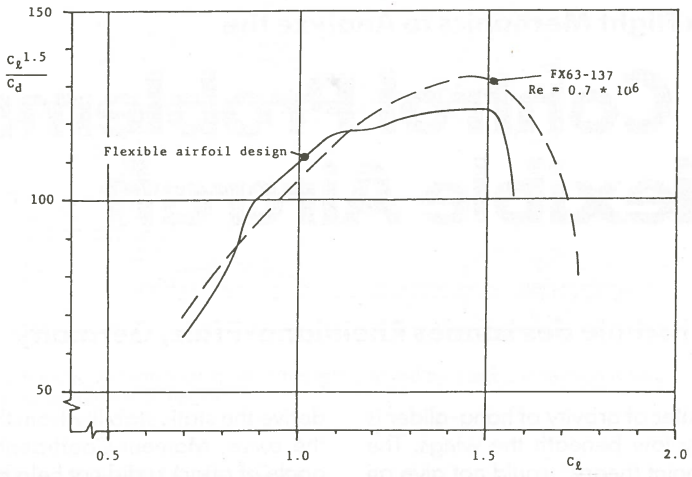

Fig. 16. Sinking speed ratio of the flexible airfoil and FX63-137.

5. References

(1) *Sweeney T.E.*, (1961) Exploratory sailwing research at Princeton. Princeton University, Dept. of Aerospace and Mechanical Sciences, Rept. No. 578.

(2) *Fink M.P.*, (1969) Full-scale investigation of the aerodynamic characteristics of a sailwing of aspect ratio 5.9. NASA TN D-5047.

(3) *Ormiston R.A.*, (1971) Theoretical and experimental aerodynamics of the sailwing. J. Aircraft, Vol. 8, No. 2.

(4) *Maughmer M.D.*, (1979) A comparison of the aerodynamic characteristics of eight sailwing airfoil sections. NASA CP 2085.

(5) *Murai H., Maruyama S.*, (1982) Theoretical investigation of sailwing airfoils taking account of elasticities. J. Aircraft, Vol. 19, No. 5.

(6) *Boer R.G. den*, (1982) Numerical and experimental investigation of the aerodynamics of double membrane sailwing airfoil sections. Delft University of Technology, Dept. of Aerospace Eng., Report LR-345.

(7) *Ingen J.L. van, Boermans L.M.M., Blom J.J.H.*, (1980) Low speed airfoil section research at Delft University of Technology. ICAS-80-10.1.

(8) *Allen H.J., Vincenti W.G.*, (1944) Wall interference in a two-dimensional flow windtunnel, with consideration of the effect of compressibility. NACA Report No. 782.

(9) *Boermans L.M.M., Terleth D.C.*, (1984) Windtunnel tests of eight sailplane wing-fuselage combinations. Technical Soaring Vol. III, No. 3.

(10) *Hoerner S.F.*, (1965) Fluid-dynamic drag. Published by the author, Brick Town, 1965.

(11) *Wortmann F.X.*, (1977) Aerofoil design for man powered aircraft. University of Stuttgart.